Tropospheric Water Vapor Transport as Determined from Airborne Lidar Measurements

ANDREAS SCHÄFLER, ANDREAS DÖRNBRACK, CHRISTOPH KIEMLE, STEPHAN RAHM,
AND MARTIN WIRTH

Institut für Physik der Atmosphäre, Deutsches Zentrum für Luft- und Raumfahrt, Oberpfaffenhofen, Germany

ABSTRACT

The first collocated measurements during THORPEX (The Observing System Research and Predictability Experiment) regional campaign in Europe in 2007 were performed by a novel four-wavelength differential absorption lidar and a scanning 2-μm Doppler wind lidar on board the research aircraft Falcon of the Deutsches Zentrum für Luft- und Raumfahrt (DLR). One mission that was characterized by exceptionally high data coverage (47% for the specific humidity q and 63% for the horizontal wind speed v_h) was selected to calculate the advective transport of atmospheric moisture qv_h along a 1600-km section in the warm sector of an extratropical cyclone. The observations are compared with special 1-hourly model data calculated by the ECMWF integrated forecast system. Along the cross section, the model underestimates the wind speed on average by -2.8% (-0.6 m s^{-1}) and overestimates the moisture at dry layers and in the boundary layer, which results in a wet bias of 17.1% (0.2 g kg^{-1}). Nevertheless, the ECMWF model reproduces quantitatively the horizontally averaged moisture transport in the warm sector. There, the superposition of high low-level humidity and the increasing wind velocities with height resulted in a deep tropospheric layer of enhanced water vapor transport qv_h. The observed moisture transport is variable and possesses a maximum of $qv_h = 130$ g kg^{-1} m s^{-1} in the lower troposphere. The pathways of the moisture transport from southwest via several branches of different geographical origin are identified by Lagrangian trajectories and by high values of the vertically averaged tropospheric moisture transport.

1. Introduction

During the last few decades, forecasts of operational numerical weather prediction (NWP) models have continuously improved as a result of an enhanced spatial resolution and advanced parameterization schemes for the model physics. Furthermore, the global coverage of spaceborne remote sensing observations and their assimilation has rapidly improved the forecast skill (Simmons and Hollingsworth 2002). However, the representation of cloud processes involving the condensation of water vapor and the associated latent heat release are thought to be a major weakness in the formulation of current operational NWP models.

The diagnosis of ''forecast–analysis'' differences of the European Centre for Medium-Range Weather Forecasts (ECMWF) Integrated Forecast System (IFS) by Didone (2006) and Dirren et al. (2003) revealed characteristic patterns of forecast errors on the downstream side of the cold front of the extratropical cyclones. Among the observational errors of the initial fields, the authors identified the inaccurate representation of diabatic effects in the IFS as a possible cause of an inaccurate cyclone forecast. An extratropical cyclone very efficiently transports moisture upward ahead of the cold front. The associated diabatic heating can, in turn, generate an upper-level negative potential vorticity (PV) anomaly, which considerably influences the large-scale dynamics and, subsequently, the precipitation distribution (Massacand et al. 2001).

Despite all of the improvements in NWP, the quantitative precipitation forecast (QPF) skill has not changed significantly in recent years. Thus, improving the QPF is one of the main research interests in numerical weather prediction (Fritsch and Carbone 2004; Rotunno and Houze 2007; Richard et al. 2007; Wulfmeyer et al. 2008). The interaction between various synoptic-scale and mesoscale processes, such as large-scale forcing (Massacand et al. 2001; Hoinka and Davies 2007), orographic lifting (Reeves and Rotunno 2008; Miglietta and Rotunno 2009), or low-level moisture supply (Boutle et al. 2010; Keil et al.

Corresponding author address: Andreas Schäfler, Institut für Physik der Atmosphäre, Deutsches Zentrum für Luft- und Raumfahrt, Oberpfaffenhofen, 82230 Wessling, Germany.
E-mail: andreas.schaefler@dlr.de

2008), and their physical representation in NWP models has emerged to play a crucial role for QPF.

In particular, the supply of low-level moisture by latent heat fluxes or through advective transport is crucial for the evolution of midlatitude weather systems. As pointed out by Boutle et al. (2010), large-scale moisture advection is the process that maintains the structure of the boundary layer in evolving midlatitude weather systems. Consequently, the large-scale and convective precipitation depend on the distribution of surface moisture and, especially, on the advective transport of water vapor. However, this key quantity lacks precise observations.

The advective moisture transport, or, more precisely, the flux of specific humidity, is the product of the magnitude of the horizontal wind velocity v_h and the water vapor mixing ratio q. Observations of this quantity require simultaneous and collocated measurements of the atmospheric variables v_h and q. Meteorological towers and airborne or balloonborne in situ observations provide this information at specific locations and along flight trajectories. However, observations covering larger areas and the complete troposphere are only possible with high-flying aircraft equipped with nadir-pointing remote sensing instruments.

During recent years, airborne lidar measurements of both wind and water vapor have been performed to investigate numerous meteorological phenomena. For example, there are studies on the boundary layer water vapor structure (Kiemle et al. 1997, 2007), on the upper-tropospheric and lower-stratospheric humidity (Poberaj et al. 2002), on the structure of stratospheric intrusions (Hoinka et al. 2003), or those revealing the mesoscale fine structure of extratropical cyclones (Flentje et al. 2005). Flentje et al. (2007) evaluated ECMWF model simulations with the differential absorption lidar (DIAL) water vapor measurements in the tropics and subtropics over the Atlantic Ocean between Europe and Brazil. A mass flux (kg s^{-1}) was calculated by Weissmann et al. (2005a) in a shallow stream toward the Alps using Doppler wind lidar (DWL) measurements.

The first collocated lidar measurements of wind and water vapor were carried out during the International H$_2$O Project (IHOP_2002) with a two-wavelength DIAL and a nonscanning DWL. Kiemle et al. (2007) used these observations to calculate profiles of the vertical latent heat flux in the convective mixing layer. Tollerud et al. (2008) used the off-nadir line-of-sight (LOS) velocity from the DWL to calculate the wind component perpendicular to the flight path. Combined with nadir-pointing DIAL measurements, they investigated the small- and mesoscale moisture transport by the low-level jet over the central Great Plains of the United States.

Here, we extend previous attempts to measure the horizontal moisture flux in the whole troposphere. For this purpose, the newly developed four-wavelength DIAL (Wirth et al. 2009) was applied for the first time to retrieve the water vapor from the lower to the upper troposphere. The scanning DWL was employed to estimate the horizontal wind components. Based on the concomitant lidar observations, a method was developed to compute vertical profiles of advective transport of water vapor. We discuss the applicability of the method based on observations carried out during the European THORPEX[1] Regional Campaign in 2007 (ETReC 2007). One of the goals of ETReC 2007 was to provide an accurate mapping of the upstream environment in coordination with the Convective and Orographically Induced Precipitation Study (COPS; see Wulfmeyer et al. 2008), which mainly focused on local convection in southwest Germany.

In accordance with the ETReC 2007 objectives, and in contrast with the spatial scales investigated by Tollerud et al. (2008), all flights were devoted to investigate the advective moisture transport in the presence of synoptic forcing, which in our case is represented by an upper-level trough over western Europe. The southwesterly flow ahead of the trough resulted in a transport of warm and humid air toward central Europe. From a total of three ETReC missions comprising seven flights, one flight was selected to demonstrate the applicability of our method. The selected measurements on 1 August 2007 had maximum data coverage of 63% and 47% for the DWL and the DIAL, respectively. Most importantly, the near-cloud-free atmosphere and the Saharan dust (see Chaboureau et al. 2010) that was embedded in the air mass facilitated lidar observations with a high aerosol backscatter throughout the whole troposphere on this particular day.

An overview of the methods used to observe wind and water vapor by the DWL and the DIAL is given in section 2. Additionally, special ECMWF forecasts are introduced for a later comparison with the observations. The method to determine the water vapor transport on a collocated grid is outlined in section 3. Furthermore, the procedure to interpolate the model fields on the collocated grid is discussed. The lidar observations of the selected research flight are presented in section 4 together with a statistical evaluation of the ECMWF model fields. The horizontal moisture transport is presented and discussed in section 5. Section 6 concludes this study.

2. Observational and model data

a. Water vapor lidar data

The DIAL technique can be applied to remotely measure atmospheric humidity with high accuracy and spatial

----

[1] The Observing System Research and Predictability Experiment (THORPEX; http://www.wmo.int/thorpex).

TABLE 1. Technical characteristics of the collocated lidar systems flown during ETReC 2007 on board the DLR research aircraft Falcon. [Avalanche photodiode (APD). Positive intrinsic negative (PIN).]

	DIAL	DWL
Transmitter type	OPO	Diode laser
Wavelength (nm)	935	2022
Pulse energy (mJ)	40	1.5
PRF (Hz)	200	500
Avg power (W)	8	0.75
Detection principle	Direct	Heterodyne
Detector type	APD	PIN diode
Telescope diameter (cm)	48	10
Horizontal resolution (s)	60	30
Vertical resolution (m)	350	100
Absolute accuracy	10%	0.1 m s^{-1}

resolution. The DIAL principle is based on the different absorption of at least two spectrally narrow laser pulses transmitted into the atmosphere. The online wavelength is tuned to the center of a molecular water vapor absorption line, and the offline wavelength positioned at a nonabsorbing wavelength serves as a reference. Airborne applications yield two-dimensional cross sections of the humidity field below the flight level.

During ETReC 2007 the new multiwavelength DIAL Water Vapor Lidar Experiment in Space (WALES; Wirth et al. 2009) was operated for the first time on board the research aircraft Falcon. The system consists of two transmitters, each of which is based on an injection-seeded optical parametric oscillator (OPO) pumped by the second harmonic of a Q-switched, diode-pumped single-mode neodymium-doped yttrium aluminium garnet (Nd:YAG) laser. The WALES laser system is capable of simultaneously emitting light at up to four wavelengths (three online and one offline) in the water vapor absorption band around 935 nm. Three different neighboring and temperature-insensitive absorption lines are selected to achieve sensitivity in the whole range of tropospheric water vapor concentrations. The entire profile is composed of the three, partly overlapping line contributions. The average output energy is 40 mJ at a repetition rate of 200 Hz (50 Hz per wavelength quadruple; see Table 1). A detailed technical description of the system is given by Wirth et al. (2009).

Like other remote sensing instruments the DIAL technique has error sources that have to be considered in the data evaluation. Both systematic and statistical errors influence the measurement accuracy (Poberaj et al. 2002). Systematic errors result, for example, from uncertainties in the spectral characteristics of the absorption lines, the limited stability of the online wavelength position, the residual temperature dependency of the absorption cross section, and the spectral purity of the laser radiation. During the ETReC 2007 flights only three out of four

possible wavelengths could be used for water vapor measurements. Additionally, the online diagnostics used to assess the spectral properties of the laser system were not yet fully implemented.

The resulting systematic uncertainty, resulting from spectral impurity of the laser, was estimated by processing the data using two spectral purities. Comparisons with radiosondes and dropsondes during ETReC 2007 revealed that 90% of the spectral purity was a good proxy. Hence, this value was used as a reference in the present study and was compared with data processed with a hypothetical spectral purity of 99%. Relative differences between the two datasets larger than 15% led to a removal of the respective data points. Additionally, the line-broadening Rayleigh–Doppler effect of scattering by air molecules was corrected with an algorithm based on the backscatter measurements. Instrumental noise causing random fluctuations of the signals can be reduced effectively by horizontal and vertical averaging. Therefore, all on- and offline signals were averaged over a certain time interval before the humidity was calculated. For this study, a horizontal resolution of 60 s ($\approx$12 km) and a vertical range resolution of 350 m were used. The systematic uncertainties and the instrumental noise are altitude dependent.

Additionally, atmospheric backscatter measurements were conducted at a wavelength of 1064 nm, generated by the pump laser, to calculate the backscatter ratio (BSR1064), which is the ratio of the total (particle and molecular) backscatter coefficient and the molecular backscatter coefficient. The resolution of the backscatter ratio is 15 m vertically and 10 s ($\approx$2 km) horizontally, with typical values ranging from 1 in a very clean atmosphere to 100 in regions with a high aerosol load.

b. Wind lidar data

The DWL provides profiles of horizontal wind direction and velocity beneath the aircraft. The system detects the frequency shift between the emitted and received signals, which is proportional to the LOS wind velocity.

The DWL consists of a diode-pumped continuous-wave master laser and a pulsed slave laser. The master laser has double importance for the system, namely for the injection seeding of the slave laser as well as for the usage as a local oscillator. The backscattered signal is mixed with the local oscillator on the detector. The resulting difference frequency is amplified and digitized. The slave laser transmits 1.5-mJ pulses at a wavelength of 2022 nm at a pulse repetition frequency (PRF) of 500 Hz (see Table 1). To retrieve a three-dimensional wind vector beneath the aircraft from LOS measurements, the system uses the velocity–azimuth display (VAD) technique. A scanner performs a conical step-and-stare scan under an off-nadir angle of 20°. The scanner stops at 24 positions

over a 360° scan (every 15°). The conical scan pattern is transformed to a cycloid pattern as the aircraft moves. A wind vector is calculated from three LOS velocities separated by 120°. In this way, eight different wind vectors are obtained per scanner revolution. First, a mean vector is calculated, and then all 24 LOS velocities are compared to the mean. Outliers are eliminated and new mean vectors are calculated repetitively until all remaining LOS velocities are situated inside a tolerance range of ± 1 m s^{-1}. The time for one scanner revolution ($\approx$30 s) and the aircraft velocity determine the horizontal resolution of the resulting wind profiles, which is about 5–10 km, depending on the distance from the aircraft. The vertical resolution of 100 m is limited by the pulse length of 400 ns (see Table 1). The PRF of 500 Hz leads to an accumulation of 500 or 1000 shots per scanner position, which is important for reducing noise. The accuracy of the wind measurements lies at $\approx$0.1 m s^{-1} at high signal-to-noise ratios. Detailed information about the DWL system, the calculation of the wind vector, and an error assessment can be found in Weissmann et al. (2005b).

c. ECMWF data

The lidar observations were compared with model fields of the ECMWF IFS in a way similar to that of Flentje et al. (2007). To cope with the continuous lidar observations, a temporal interpolation of the model data was necessary. Because a linear temporal interpolation of the operational 6-hourly analysis interval does not resolve a nonlinear evolution of the weather systems, short-term forecasts were performed with the IFS. For these special forecasts the latest model version at a T799L91 resolution, equivalent to 799 linear spectral components and 91 vertical levels, was used.

The special short-term forecasts were initialized with the available operational analyses at 0000, 0600, 1200, and 1800 UTC 1 August 2007, and the output was stored in 1-hourly intervals up to +5 h. The operational analyses and the four daily forecast runs were combined to generate a uniform 1-hourly temporal resolution of the ECMWF model fields. In that way, even regions where a noneven (nonlinear) evolution occurred (e.g., at fronts) are relatively well represented in the composed model fields, so that observed areas with strong spatial humidity and wind gradients can be compared to the model output with higher confidence. The resulting model data were interpolated on a regular 0.25° × 0.25° grid corresponding to a horizontal grid spacing of about 25 km.

3. Methods

Both the DIAL and the DWL sample different volumes in the atmosphere. The wind profiles result from conical scans of the DWL, whereas the water vapor profiles result from the nadir-pointing DIAL. To calculate the horizontal transport from the observed wind and humidity fields both datasets had to be interpolated onto a grid where all data points are collocated. In a further step, results from the numerical weather prediction model were also interpolated onto this collocated lidar grid in order to facilitate the comparison between the lidar measurements and the model products.

a. Interpolation of lidar data to a collocated grid and transport calculation

The DIAL and the DWL data were averaged over approximately 60 and 30 s, respectively. This means that the horizontal displacements between successive profiles vary in time as a result of the variable speed of the Falcon. These profiles have a vertical uniform spacing of 150 (DIAL) and 100 (DWL) m, respectively. The collocated lidar grid was defined as a regular mesh with uniform resolutions of $\Delta t = 30$ s and $\Delta z = 100$ m, respectively. Both two-dimensional data matrices from the DIAL and DWL were interpolated bilinearly to the collocated lidar grid. Longitude and latitude positions of the collocated profiles were linearly interpolated from the aircraft GPS data associated with the observations. The temporal interval between the profiles on the collocated grid corresponds approximately to the original resolution of the wind observations. In this way, the wind measurements were not truncated by the bilinear interpolation.

Depending on specific requirements, the values on the collocated lidar grid can subsequently be averaged to coarser vertical or horizontal resolutions. We calculated the advective moisture transport as the product of specific humidity q and the magnitude of the horizontal wind velocity v_h (g kg^{-1} m s^{-1}) on the collocated lidar grid.

b. Interpolation of model data to the collocated lidar grid and intercomparison

In a first step, the ECMWF analysis and forecast fields at every model level and at all relevant times were spatially interpolated to the horizontal positions of the flight track. These locations were defined by the latitude and longitude of the collocated lidar grid. As before, bilinear interpolation was used to interpolate ECMWF output quantities from four surrounding model grid points to the collocated lidar grid positions. The results were two-dimensional cross sections of the ECMWF profiles along the flight path from the surface up to the highest model level for each analysis and forecast time. In a second step, the cross sections at the different forecast or analysis times were linearly interpolated to the respective time of the observation. In a final third step, a linear interpolation
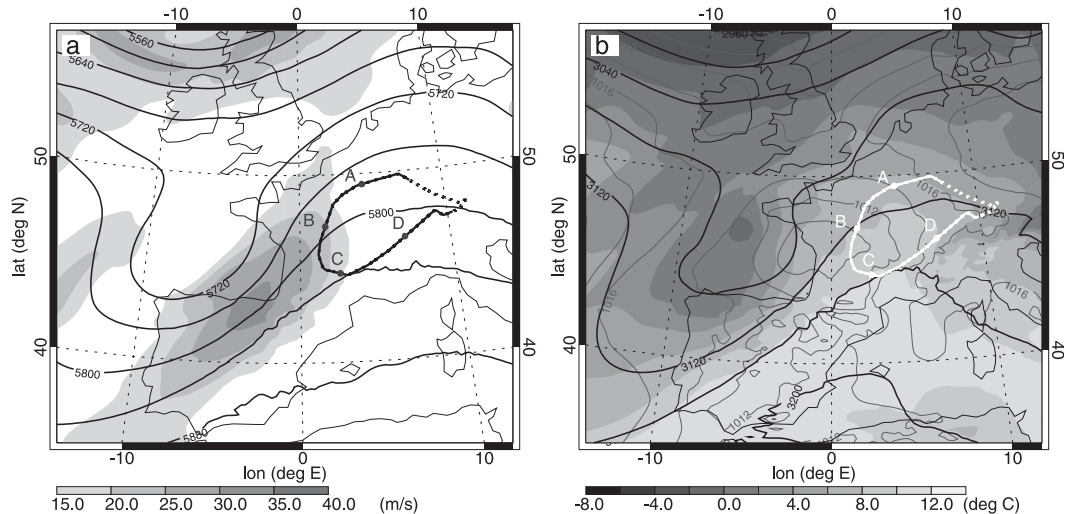
FIG. 1. ECMWF analysis valid at 1200 UTC 1 Aug 2007. (a) Geopotential height (m, black lines) and horizontal wind speed (m s^{-1}, shaded areas) at 500 hPa. (b) Mean sea level pressure (hPa, dark gray lines), geopotential height (m, black lines), and temperature (°C, shaded) at 700 hPa. The black and white lines in (a) and (b) show the flight track of the DLR Falcon whereby the solid line segment indicates the period of collocated lidar measurements. Points A–D indicate the positions of the aircraft every 30 min, beginning at 1530 UTC (point A).

of the model-level data to the vertical locations of the collocated lidar grid was performed. For this purpose, the geometrical height of the model surfaces had to be calculated by integrating the hydrostatic equation. At the end of these three steps, model data and measured data were arranged on the same grid for further calculations.

One main issue of the present study is the calculation of deviations between the measured quantities and the model fields. Here, we present two measures for the deviation, an absolute difference (AD) and a relative difference (RD), as proposed by Flentje et al. (2007). Using the water vapor as an example, the AD (g kg^{-1}) was calculated as $q_{ECMWF} - q_{LI}$ and RD (%) as $[q_{ECMWF} - q_{LI}/(q_{ECMWF}/2 + q_{LI}/2)]100$. Generally, positive AD or RD values are equivalent to overestimated simulated moisture, whereas negative values indicate a dry bias in the model.

4. Lidar observations and comparison with ECMWF model output

a. Flight pattern and meteorological conditions

Figure 1 depicts the synoptic situation on 1 August 2007 at 1200 UTC and the track of the research flight that was performed between 1430 and 1730 UTC. After take-off in Oberpfaffenhofen (48.1°N, 11.3°W), Germany, the DLR Falcon flew northwestward over Germany and turned anticlockwise at about 50°N toward Paris, France. There, the aircraft continued on a southward leg to the Massif

Central from which it returned to Oberpfaffenhofen, passing the Rhône Valley and the Swiss alpine region.

At 1200 UTC 1 August 2007 (2.5 h before departure), the large-scale flow pattern at the 500-hPa pressure surface shows a trough over the southern Bay of Biscay (see Fig. 1a), which moved westward during the day. On its eastern flank a surface low below a strong jet streak intensified during the day. In Fig. 1b the low is located at about 46°N, 0°E and moved northeastward in conjunction with the propagating trough. During the same time period, an ongoing southwesterly flow advected warm and moist air masses toward central Europe. The large-scale advective moisture transport favored the development of the unstable environment over southwestern and central France. There, a strong convective event occurred in the evening hours in conjunction with a surface convergence zone and the upper-level forcing.

The equivalent potential temperature chart at 700 hPa (see black contour lines in Fig. 9) reveals that the associated frontal system comprised a short occluded part north of the center of the low and a southwest-to-northeast-oriented cold front west of the flight path. A warm front separated the southerly warm and moist air from the cold and dry air over northeastern Europe (see the temperature field in Fig. 1b). Along the flight track, the lidars observed the pronounced moisture gradient at the warm front twice (at 700 hPa between points A and B, and C and D, respectively) and detected the moisture advection ahead of the arriving cold front over southwestern France (see Fig. 9).
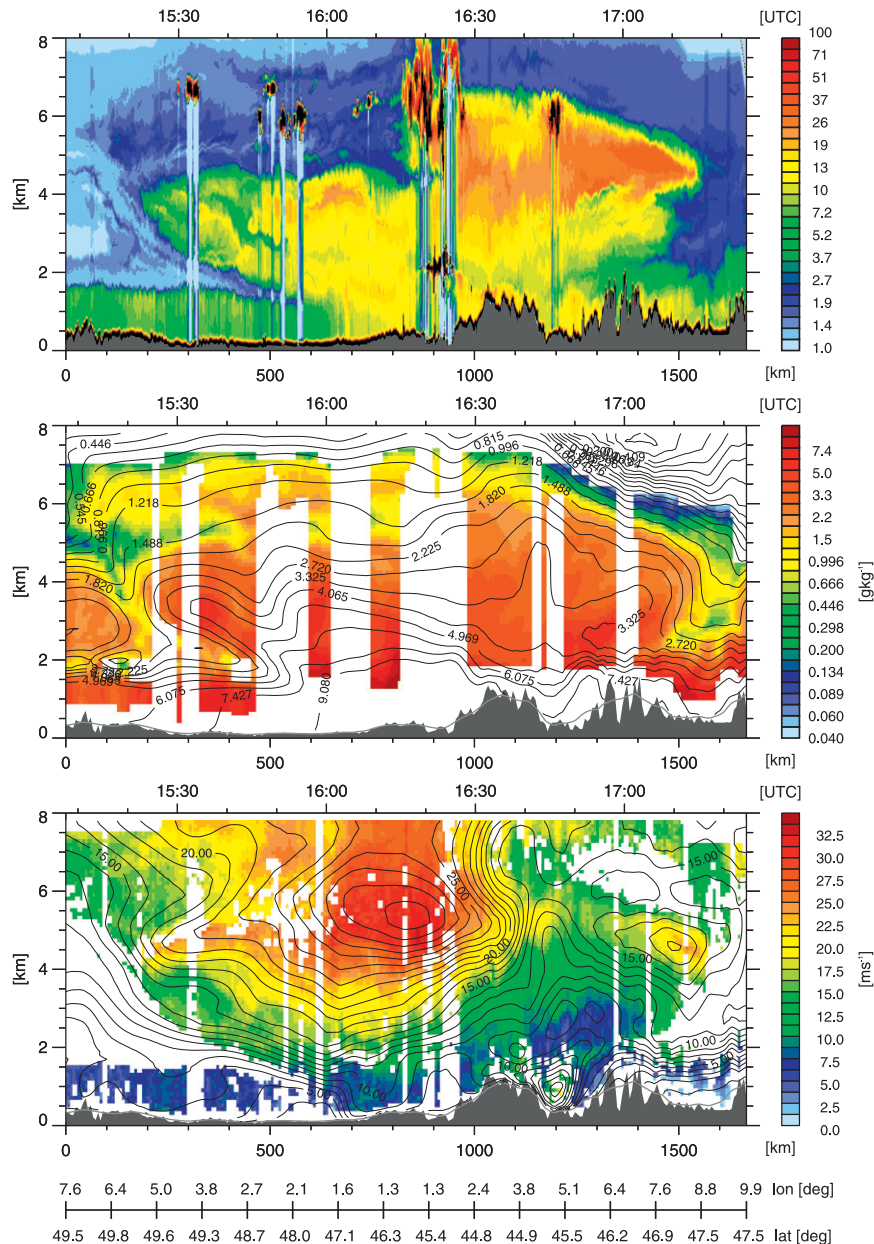
FIG. 2. Lidar measurements on 1 Aug 2007 of (top) atmospheric backscatter ratio BSR1064 in logarithmic scale; (middle) specific humidity q (g kg^{-1}) in logarithmic scale, superimposed with contour lines of ECMWF short-term forecast and analysis data; and (bottom) horizontal wind speed v_h (m s^{-1}), superimposed with ECMWF isotachs. Dark gray areas represent topography below the flight track interpolated from the Global Land One-Kilometer Base Elevation (GLOBE) digital elevation model (DEM; GLOBE Task Team 1999); the light gray line marks the topography interpolated from the ECMWF model.

b. Interpretation of wind and water vapor fields

Figure 2 shows the lidar cross sections of BSR1064, the water vapor mixing ratio, and the horizontal wind velocity superimposed with contours of the ECMWF model fields. The displayed topography with rather flat terrain during the first part of the flight corresponds to the northern part of the loop (see the solid track line in Fig. 1), where the region of Paris (48.6°N, 2.5°E) was reached at ≈1545 UTC. At ≈1630 UTC (44.7°N, 2.6°E; point C in Fig. 1), the topography indicates the elevations of the Massif Central. After passing the Rhône Valley, the Falcon flew over the Alps at ≈1700 UTC (46.5°N, 7.0°E; point D in Fig. 1).

We start the discussion of the lidar observations with the BSR at 1064 nm (Fig. 2, top panel). At the beginning of the flight, a well-mixed boundary layer (BSR1064 ≈ 5) with an upper lid at ≈1800 m above ground was observed by the DIAL. Above the sharp aerosol gradient, clean tropospheric air (BSR1064 < 2) dominated the backscatter signal. As the aircraft turned gradually southward, the lidar detected an elevated aerosol layer (dominated by Saharan dust), which extended up to 4500-m altitude. This observed wedge-shaped structure belongs to one branch, namely the western part of the tilted warm front. The aerosol load increased from the well-mixed boundary layer into this warm front air mass, which is reflected by the enhanced BSR1064 ≈ 12 [see Fig. 2, top panel, ≈ 1600 UTC, (47.3°N, 1.7°E), point B]. About 2 km above the wedge-shaped aerosol layer a few isolated spots of clouds appear in the backscatter signal with BSR1064 ≈ 100. In the southwestern part of the flight track (between points B and C, at 1600–1630 UTC) upper-tropospheric clouds prevented DIAL observations for about 15 min. After the short data gap underneath these clouds, the eastern part of the warm front with an elevated and thicker aerosol layer was sampled after point C. This part of the warm front possesses a higher aerosol load that is reflected in BSR1064 values of up to ≈40 (Fig. 2, top panel). Below the elevated aerosol layer, a gradual transition in terms of BSR1064 to the heterogeneous boundary layer over the Alps was observed near point D. The nose of the elevated aerosol layer on the eastern side of the warm front was located over the northern alpine region at ≈4.5 km above MSL.

Figure 2 (middle panel) shows the observed water vapor distribution. The well-mixed boundary layer in the first flight segment until point B is characterized by a specific humidity $q \approx 7$ g kg^{-1}. The PBL is capped by a narrow dry layer ($q \approx 1$ g kg^{-1}), which corresponds to minimum BSR1064 values. Above the PBL, moist air ($q \approx 2.5$ g kg^{-1}) extends up to ≈5-km altitude above ground, again associated with low BSR1064 values [before 1520 UTC, (49.6°N, 5.1°E)]. In contrast to the air mass northeast of the warm front, the adjacent coherent moist layer belongs to the warm sector. The largest observed and simulated q values of up to 11 g kg^{-1} occurred at about 2-km altitude about halfway between points B and C. The shape of the moist layer coincides with enhanced BSR1064 values (see Fig. 2, top panel). For instance, the top height of the moisture layer decreases toward the end of the flight in accord with the sloped aerosol layer. However, in the first segment of the flight path (up to point C) an upper-level moist layer was observed in a region with low aerosol content between 5.5 and 7.5 km MSL.

The magnitude of the horizontal wind vector v_h along the flight track is shown in Fig. 2 (bottom panel). The wind distribution is dominated by the strong maximum of the jet stream, which was approached in the southwestern part of the flight. The order of magnitude of the observed maximum values of up to 30 m s^{-1} at ≈1625 UTC (45.0°N, 1.8°E) correspond to the analyzed horizontal wind velocity at the 500-hPa level (≈5.8 km) of the ECMWF some hours before (Fig. 1a). Because of the curved flight path, the decline of wind velocities on either side of the maximum in Fig. 2 actually corresponds to a decrease in v_h toward the northeast. At the end of the flight (after point D) a second local wind speed maximum occurred on the tip of the aerosol nose at ≈4.5 km above the ground. At lower levels, the boundary layer flow was generally characterized by low wind velocities, except for a strong wind maximum resulting from a canalization effect in the Rhône Valley (only visible from superimposed ECWMF contours) at ≈1645 UTC (45.4°N, 4.8°E). The wind direction along the flight path was predominantly southwest (not shown). Only at the beginning and at the end of the flight, the upper-level ridge caused westerly wind directions. This is consistent with the lower aerosol load in these segments and points to the different origins of the air masses during the flight. In the boundary layer, the surface low (see Fig. 1b) induced southerly wind directions located between points A and C as well as in the Rhône Valley.

In summary, the spatial structure of the water vapor field suggests that moist air from the south glided above a well-mixed boundary layer that developed over northeastern France during the day. The tilted warm front is displayed by an intrusion-like humidity gradient in both segments of the observed warm front in Fig. 2. This ascending warm air is also reflected in the BSR1064 observations that show a distinct separation of aerosol-rich air in the warm sector, and nearly aerosol-free air in the northeastern parts of the flight. High southwesterly winds indicate strong advection of moisture toward central Europe.

c. Model comparison

Despite the qualitatively good reproduction of the observed wind and water vapor structures by the superimposed ECMWF analyses, for example, the warm front moisture gradients or the wind velocity maxima (see Fig. 2), some smaller-scale features are insufficiently reproduced.

Figure 3 shows cross sections of AD and RD. The highest absolute deviations occurred predominantly in the lower troposphere. The maximum absolute deviations $AD_{min} = -2.8$ g kg^{-1} and $AD_{max} = 4.5$ g kg^{-1} are located in the moist air mass at the warm front (see Fig. 3a; 1645–1700 UTC at 2–3 km MSL) and at the region of maximum observed humidity (see Fig. 3a; 1605–1620 UTC at 1–3 km MSL), respectively. The largest positive relative deviations ($RD_{max} = 172\%$; see Fig. 3b) that indicate a
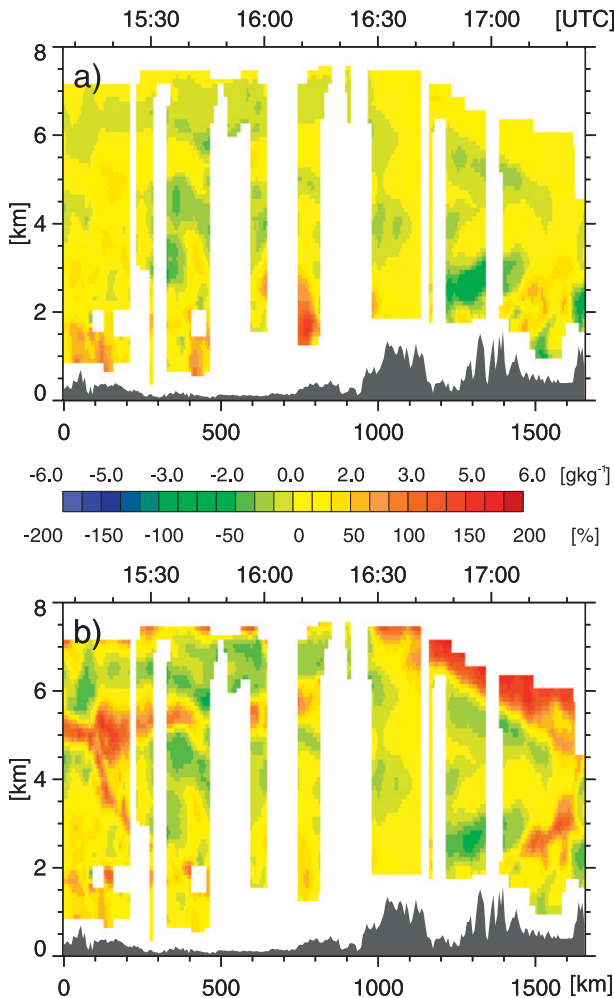
FIG. 3. (a) Absolute (g kg^{-1}) and (b) relative differences (%) of water vapor between ECMWF simulations and DIAL observations on 1 Aug 2007. Topography as in Fig. 2.

moist bias occur in insufficiently represented dry layers and strong gradients in the upper troposphere at low moisture contents and indicate a moist bias. On the other hand, the most negative relative deviation (RD_{min} = -60%) occurred at the warm front boundary surface in the lower troposphere (see Fig. 3a; 1645–1700 UTC at 2–3 km MSL).

Figure 4 illustrates a statistical comparison of the humidity with the ECMWF model simulation as described in section 3 for the entire cross section of Fig. 3. The left panel of Fig. 4 shows the scatterplot of the observed and the simulated specific humidity with gray-shaded altitude information. The mean absolute deviation of 0.2 g kg^{-1} and the corresponding mean relative bias of 17.1% indicate an overestimated specific humidity in the ECMWF model fields. In particular, very low humidity values were insufficiently reproduced by the model, which can be detected by the large number of points above the 45° line. The correlation of the two datasets is 91%.

The middle panel of Fig. 4 shows the AD and RD frequency distributions. In contrast to the roughly symmetric AD distribution, the RDs are asymmetrically distributed, which results from an accentuation of higher deviations at low humidity values.

The right panel of Fig. 4 shows the vertical distribution of both types of deviations and the data availability. Above the boundary layer, which has a rather low data density, a layer with nearly uniform data coverage of ≈60% extends up to ≈7 km. In the lowermost 2 km, significant horizontal mean ADs up to 1.9 g kg^{-1} indicate an overestimated model humidity in the boundary layer and the area of highest moisture in the southwest of the flight pattern (see Fig. 3a; 0–2 km MSL between 1510 and 1615 UTC). Above 2 km the AD values decrease quickly and become slightly negative at ≈4.5 km below a second maximum (≈0.4 g kg^{-1}) at 5.5-km altitude. This error pattern stands out more clearly in the relative deviations. It is strongly influenced by the overestimated humidity at the top edge of the eastern warm front and the unrepresented dry layer on the first part of the flight (see Fig. 3). Above 6 km these deviations are reduced by negative values occurring above the unrepresented dry layer in 5.5–7-km altitude (see Fig. 3a; 1510–1620 UTC). The shaded area indicates the total lidar accuracy, including systematic and noise-induced uncertainties, and confirms the reliability of the increased deviations in the lowest 2 km. Above that layer, the AD lies in the range of the measurement uncertainty, but admittedly the deviations and the uncertainty are small. The reduced data coverage of 47% is a result of data gaps occurring during curve flights, beneath optical thick clouds and close to the ground.

Figure 5 shows the deviations of the wind velocity. The regions with maximum overestimation occurred in the Rhône Valley (AD = 7.8 m s^{-1}, RD = 100%; see Figs. 5a,b at ≈1 km MSL around 1640 UTC). Between 1640 (45.0°N, 4.1°E) and 1645 (45.5°N, 4.8°E) UTC large negative deviations of up to -8.8 m s^{-1} at ≈ 5 km above MSL point to an observed wind maximum that is not reproduced by the ECMWF model fields.

Modeled and observed wind velocities are more evenly distributed in the scatterplot, as shown in Fig. 6, and have a slightly higher correlation of ≈96%. The mean wind velocity was 17.5 m s^{-1} and the highest values (up to ≈33 m s^{-1}) appeared around 5.5 km corresponding to the jet stream wind maximum as depicted in Fig. 2. It was found that the model underestimates the highest wind velocities because the highest values are consistently situated below the ideal 45° line. The slight negative bias of -0.6 m s^{-1} (-2.8%) indicates an underestimation of the wind
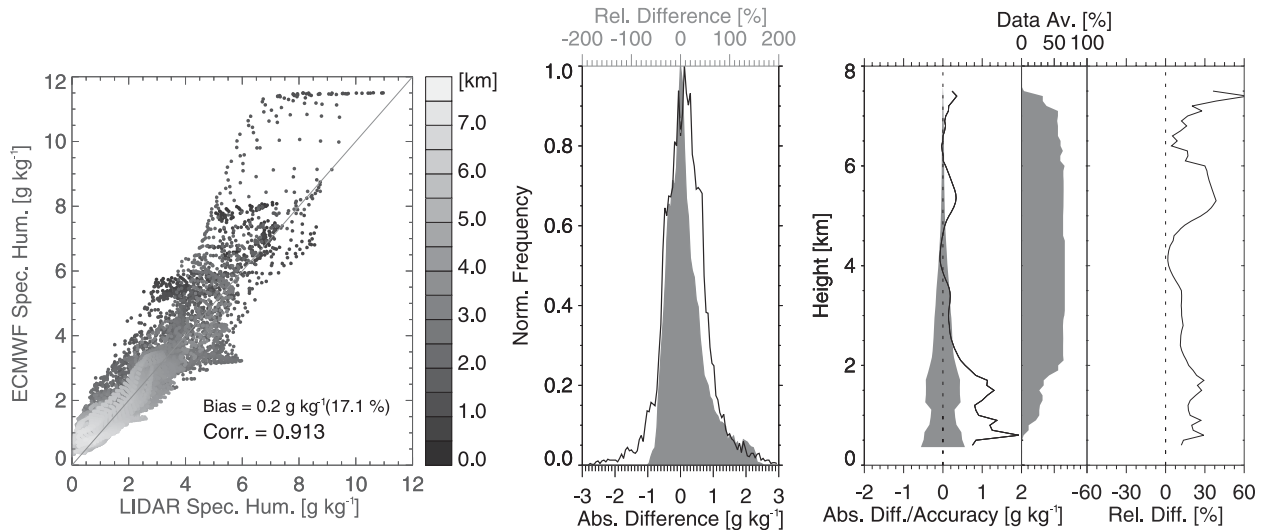
FIG. 4. Statistics of observed and modeled specific humidity on 1 Aug 2007. (left) Scatterplot of all data points with gray-shaded height information. (middle) Normalized frequency distributions of AD (g kg^{-1}, black line) and RD (%, gray shaded area). (right; from left to right) The horizontally averaged AD (g kg^{-1}, black line) and DIAL measurement accuracy (g kg^{-1}, gray shaded area), the vertical data availability (%, gray shaded area), and the horizontally averaged RD (%, black line).

velocity. Similar to the humidity deviations, the absolute wind deviations show a symmetric frequency distribution. However, the relative deviations differ because they possess a very narrow frequency distribution compared to the specific humidity. The regions with maximum overestimation in the Rhône Valley are reflected in the positive values of the horizontal mean deviations between 0.5 and 1.5 km (Fig. 6, right panel). The small maximum, which was not simulated, influences the vertical distribution of the mean absolute deviations at ≈5 km. In contrast to the water vapor deviation, those RDs of the wind are small, except for some higher values close to the ground where the data density is low. The overall data availability for the wind measurements is ≈61% and increases both with altitude and with the horizontal extent of the aerosol layer. The enhanced aerosol backscattering in the mixed boundary layer increases the amount of wind data up to 1.5 km MSL.

5. Horizontal moisture transport

As outlined in section 4b, moist air was advected from the southwest toward central Europe before and during the research flight. The moisture supply was a main ingredient for the development of a mesoscale convective system that appeared a couple of hours after the airborne observations. In the following, we discuss the spatial and temporal evolution of the water vapor transport with regard to the collocated measurements.

Figure 7 shows the magnitude of the horizontal moisture transport qv_h calculated from the collocated lidar

measurements. For both lidars data gaps appear at different locations (see Figs. 2b,c). Therefore, altogether ≈33% of the potential observations could be used to estimate the horizontal moisture transport. In the free troposphere typical values of qv_h are very variable and range between 20 and 100 g kg^{-1} m s^{-1}. Various spots with maximum values of up to 125 g kg^{-1} m s^{-1} occur in a 2-km-deep layer below the jet stream between 1550 and 1620 UTC. The moisture transport maximum results from the combination of high-tropospheric humidity values and the increasing wind velocity with height.

The moisture transport occurred at different spatial scales. The dominating large-scale transport was associated with the jet stream and occurs in the warm sector in advance of the approaching cold front. A sharp horizontal qv_h gradient extends up to 4 km MSL and marks the wedge-shaped warm front before point B (1600 UTC). In contrast, the measurements after point C (1630 UTC) reveal noticeably smaller qv_h values and a weaker gradient at the warm front. In the lower troposphere, the ECMWF analyses as well as some observations show regions of moisture transport on a smaller scale. For example, in the Rhône Valley, the maximum of $qv_h = 130$ g kg^{-1} m s^{-1} is only identifiable in the model contours. This maximum of horizontal transport is due to high wind speeds (canalization) and high humidity values in the valley. On the other hand, the weaker transport maximum (≈45 g kg^{-1} m s^{-1}) in the boundary layer at around 1610 UTC appears to be due to the presence of high humidity values in a region of relatively weak winds.
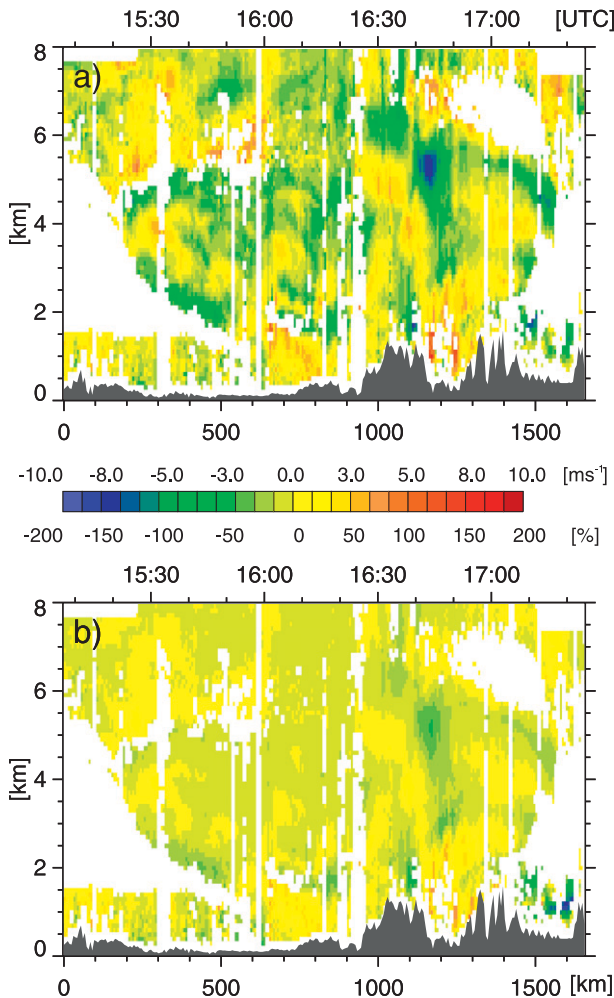
FIG. 5. (a) Absolute (m s^{-1}) and (b) relative differences (%) of the horizontal wind velocity between ECMWF simulations and DWL observations on 1 Aug 2007. Topography as in Fig. 2.

The right panel of Fig. 7 shows averaged vertical profiles of the horizontal moisture transport as calculated from lidar (dotted contour line) and ECMWF data (solid black line). The ECMWF mean profile was averaged over all points where concomitant lidar measurements exist. Its magnitude and shape agree surprisingly well with the lidar observations. The mean transport is nearly constant ($\approx$40 g kg^{-1} m s^{-1}) below the elevated maximum ($\approx$80 g kg^{-1} m s^{-1}) at 1.8-km altitude. However, the local maximum is an artifact of the few observations dominated by high transport values (see the minimum in the data coverage in Fig. 7). Above this maximum, the transport gradually decreases with altitude. In the lowest 1.5 km of the boundary layer the ECMWF overestimated the transport on average by $\approx$6 g kg^{-1} m s^{-1} ($\approx$16%). The layer above 2.5-km altitude only shows small negative differences ($\approx$2 g kg^{-1} m s^{-1}, or $\approx$5%).

Admittedly, these mean profiles are not representative for an average moisture transport in the warm sector. That quantity can only be calculated from the ECWMF analyses and is shown in Fig. 7 (cf. red line), which displays a nearly uniform value of $\approx$60 g kg^{-1} m s^{-1} between 0.5- and 2-km altitude. Remarkably, all three mean profiles are very close above 2-km altitude. Therefore, the lidar measurements provide a representative estimate of the mean transport for this specific case.

To discuss the temporal evolution of the transport, Fig. 8 shows 3-day Lagrangian trajectories covering the period from 0000 UTC 31 July to 0000 UTC 3 August. They were calculated with the Lagrangian Analysis Tool (LAGRANTO; Wernli and Davies 1997) using meteorological data from operational ECMWF analyses. The parcels were transported forward and backward in time. They departed from the locations and times of eight selected lidar profiles and were distributed at nine vertical levels in the region with maximum transport defined as $qv_h > 85$ g kg^{-1} m s^{-1} (see bold line in Fig. 7). In the composed trajectories, the aircraft measurements appear from 38.5 to 41.5 h, as indicated by the gray bar in Fig. 8. The color grading of the trajectories represents the increasing initial altitude on the cross section at the start time.

Generally, the air masses originated from three different geographical regions: one located over the Mediterranean, another over the Iberian Peninsula, and a third over the Atlantic Ocean. Before the time of the airborne observations, most of the parcels were transported at low altitudes beneath 800 hPa. Trajectories marked by red and orange colors most of the time remained close to the ground and possessed maximum humidity values (see Fig. 8, lower panels). The blue trajectories crossed the flight path at the highest altitudes comprising the lowest humidity contents. The water vapor transport calculated along the trajectories increased toward the observation time where values between 85 and 110 g kg^{-1} m s^{-1} were obtained (see Fig. 8, bottom panel).

After the observational period, the trajectories marked in green and blue experienced the largest synoptic-scale ascent, which was accompanied by a decrease of moisture. The ascent in a nearly coherent band resembles a warm conveyer belt signature with its northeasterly flow along the jet stream (see Fig. 8, top panel). Additionally, condensational processes in the convective clouds that appeared some hours after the flight may have influenced the ascent and the moisture reduction. The moisture transport values increased for about 4 h after the trajectories passed the observational window and subsequently decreased, at first rapidly and then in a more gradual way, to values below 30 g kg^{-1} m s^{-1} at 72 h. Parts of the trajectories initialized at the lowest levels stayed below 700 hPa, and the respective air parcels veered to the east
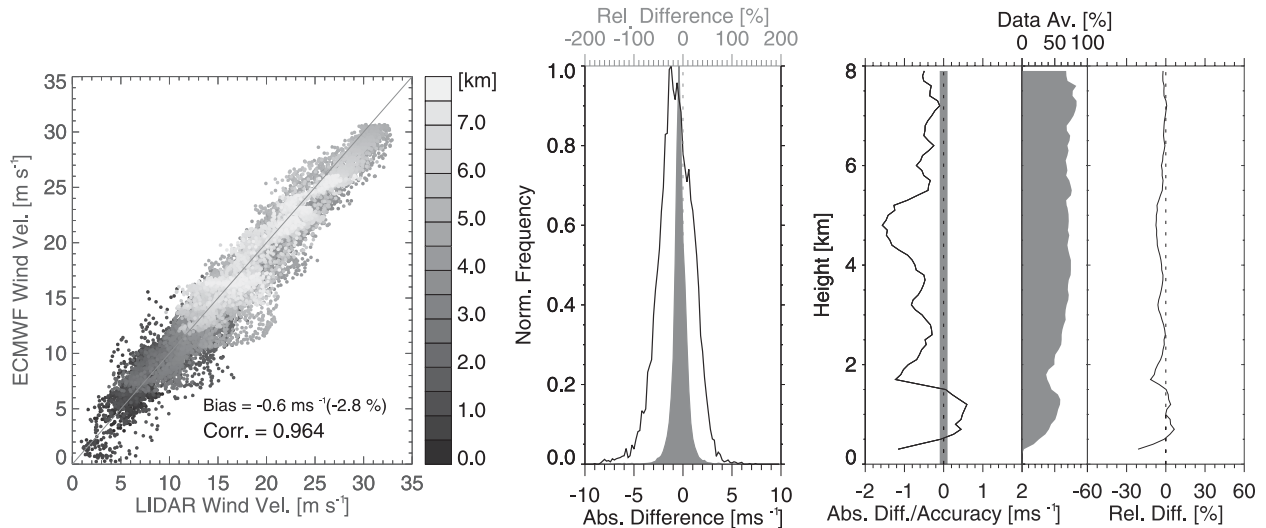
FIG. 6. As in Fig. 4, but for wind observations and simulations.

of the coherently ascending band. Those parcels also retained the bulk of their initial moisture content and the transport varied at values above $qv_h > 40$ g kg^{-1} m s^{-1}.

To produce a composite of the different moisture pathways, Fig. 9 shows the vertically averaged horizontal transport of moisture valid at 1500 UTC and calculated from a 3-h ECMWF forecast. The maximum layer mean transport values of $qv_h \approx 70$ g kg^{-1} m s^{-1} are aligned with the cold front (see equivalent potential temperature contours in Fig. 9). Additionally, increased transport values appear in the entire warm sector and, additionally, westward of the cold front. There are three main moisture pathways: From the southeast, moisture is fed into

the warm sector in the region of the Garonne Valley. The second pathway over the Pyrenees consists of several smaller branches. Finally, moisture is also supplied over the Bay of Biscay north of the Iberian Peninsula. These pathways retrieved from a vertically averaged Eulerian variable (moisture transport qv_h) are also identifiable in the Lagrangian trajectories, as shown in Fig. 6. This reveals that the temporally increasing moisture transport before the observations (see Fig. 6) develops along the identified pathways.

Although Fig. 9 only provides a snapshot close to the time of the aircraft observations, analysis times before and after 1500 UTC reveal the same moisture pathways.
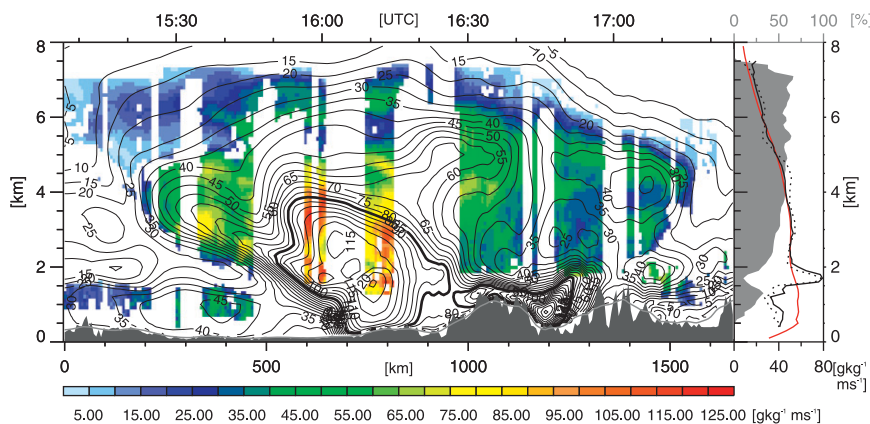

FIG. 7. Horizontal transport (g kg^{-1} m s^{-1}) calculated from lidar observations on 1 Aug 2007. (left) Moisture transport (g kg^{-1} m s^{-1}) superimposed with contour lines of ECMWF short-term forecast and analysis data. The 85 g kg^{-1} m s^{-1} contour is indicated (bold line). Topography is as in Fig. 2. (right) Horizontally mean transport (g kg^{-1} m s^{-1}) profiles of lidar (black dashed line) and ECMWF (black solid line) at points with available lidar data. ECMWF horizontally mean transport (g kg^{-1} m s^{-1}, red solid line) of all points on the collocated grid. Data availability as a function of height (%, gray shaded area).
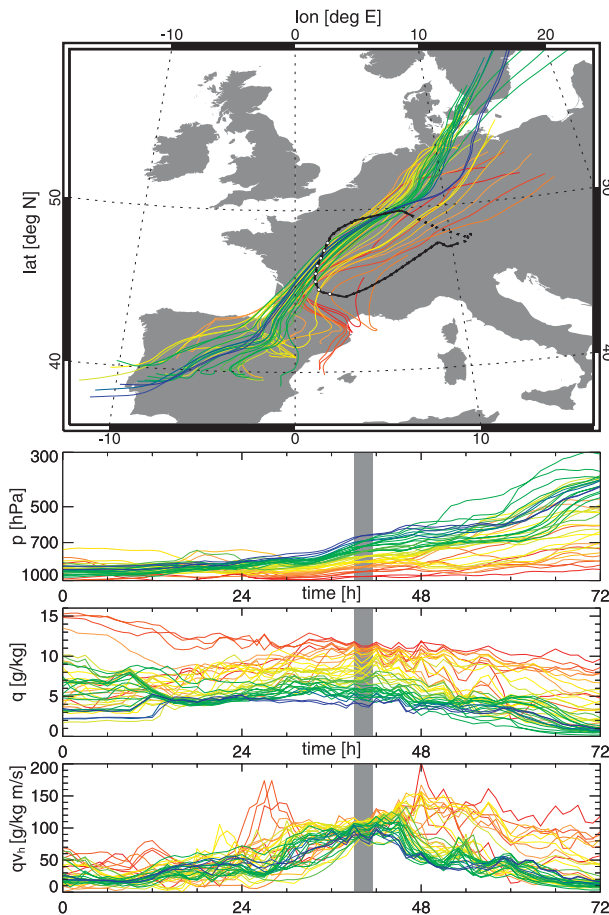
FIG. 8. Combined forward and backward trajectories starting along the flight track between 1430 and 1730 UTC 1 Aug 2007 (as indicated by the gray bar in the lower panels). The departure points are locations along the flight track (indicted by the dots in the upper panel) in the southwestern part of the flight where maximum transport ($qv_h > 85$ g kg^{-1} m s^{-1}) occurred at 10 vertical levels and at 10 profile locations. Parcel trajectories are color coded in dependence of the pressure at the time of the observation. (top) Locations of the trajectories, and (bottom) temporal development of pressure, specific humidity, and transport qv_h.

Because of the synoptic evolution, the magnitude of the moisture transport in the warm sector grows during the day (not shown). The time window and the flight track were optimally chosen because the region with maximum water vapor transport could be sampled by remote sensing instruments before the appearance of convective clouds.

6. Conclusions

The evolution of midlatitude weather systems is influenced by the supply of low-level moisture either by latent heat fluxes or through advective transport. Airborne observations of horizontal wind and water vapor profiles along extended flight legs are necessary to calculate the
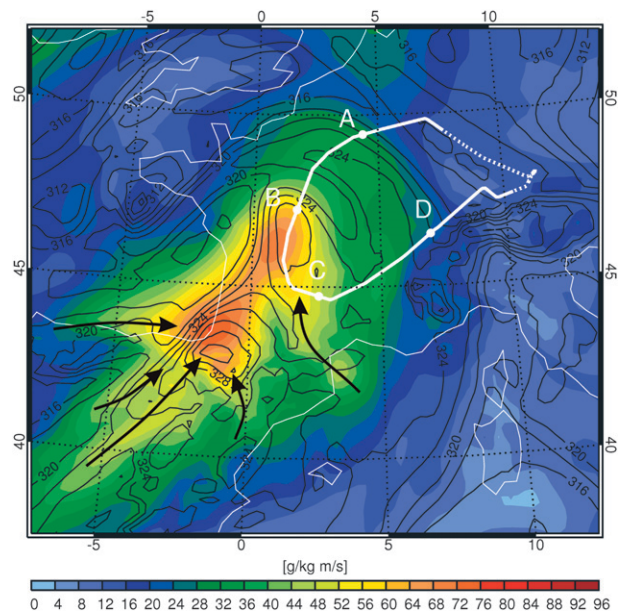

FIG. 9. ECMWF forecast (initialization at 1200 UTC 1 Aug 2007) valid at 1500 UTC 1 Aug 2007 for mean horizontal transport averaged over a layer between the ground and 8 km (g kg^{-1} m s^{-1}, shaded) and equivalent potential temperature (K, black lines.) The white line shows the flight pattern of the DLR Falcon, where the solid line indicates the section of collocated lidar measurements. Points A–D indicate the position of the Falcon every 30 min, beginning at 1530 UTC (point A). The black arrows mark the main transport pathways (see section 5).

large-scale horizontal transport. In this case study, we presented a method to quantify the advective moisture transport in a warm sector of an extratropical cyclone based on collocated lidar observations.

Special missions were devoted to observing the large-scale moisture transport during ETReC 2007 by deploying the DLR research aircraft Falcon. For the first time, the newly developed nadir-pointing multiwavelength DIAL WALES (Wirth et al. 2009) and the scanning DWL performed simultaneous measurements of water vapor and horizontal wind speed. Out of seven ETReC missions, one case was selected because it provided the unique opportunity to observe both quantities in unprecedented detail inside the warm sector. Under the nearly cloud-free conditions an exceptionally high 47% DIAL coverage was obtained. Yet, even higher data coverage of nearly 63% was attained by the DWL resulting from the additional high aerosol load of the air mass. However, because of the different sensitivity of both instruments, the data available for the transport calculations amounted to 33%.

Because the observational data only covered some parts of the sampled warm sector, meteorological model output was produced to interpret the data. For this purpose, special short-term ECWMF forecasts with 1-hourly output

were performed. Such high-resolution model output is important to capture the complex structure at frontal boundaries.

Both the model data and the observational data were interpolated onto a common collocated grid to facilitate their comparison and the calculation of the horizontal moisture transport. A comparison of the model fields with the observations revealed a bias of -0.6 m s^{-1} (-2.8%) for the wind velocity and 0.2 g kg^{-1} (17.1%) for the humidity. The model slightly tends to underestimate the wind velocity in this complex dynamic structure. The wet bias of the model results from inadequately reproduced gradients, from dry layers, and from a too-moist boundary layer. This finding is consistent with results obtained by Flentje et al. (2007), who reported a maximum moist bias of 11% in the subtropical and tropical Atlantic regions. However, the results are difficult to compare because their flights took place over the Atlantic Ocean in contrast to the measurements presented here, which were collected over western Europe.

The main focus of this paper was to quantify the moisture transport qv_h because this value crucially impacts the development of extratropical cyclones and the initiation of convection in prefrontal areas. In the sampled warm sector of the extratropical cyclone, the superposition of high humidity values at lower levels and the increasing wind velocities with height resulted in a deep tropospheric layer of enhanced water vapor transport qv_h. There, a wide range of qv_h values occurred with maximum values up to 130 g kg^{-1} m s^{-1}. Representative vertical profiles of the mean moisture transport inside the warm sector were calculated from model and observational data. At altitudes with data coverage larger than $\approx 50\%$, the experimentally determined mean transport represented the modeled value with high accuracy for this specific case. Most impressively, the flow in the warm sector as represented by enhanced water vapor transport as shown in Figs. 7 and 9 resembles an "atmospheric river" [see the conceptual model by Ralph et al. (2004); their Fig. 23]. Therefore, the moisture transport observation in Fig. 7 was suitable for visualizing the fine structure of this flow characterized by large horizontal gradients at the warm front. We found that the increased vertically integrated water vapor transport (see Fig. 9) along the atmospheric river was fed by several branches. The inflow from the southwest was confirmed by Lagrangian trajectories that were initiated along the cross section at locations of maximum moisture transport.

Although only 33% of our data could be used to calculate the horizontal moisture transport, the airborne lidar instruments confirmed their usefulness for case studies dealing with the complex dynamic structure of the warm sector. Especially, the combination with numerical model data constitutes a basis for a more complete and detailed picture of three-dimensional moisture transport. Therefore, collocated airborne lidar measurements of specific humidity and wind offer a great potential for upcoming field studies dealing with dynamical processes. For example, in an ongoing project, the method to calculate the advective moisture transport is used to analyze the inflow region of a warm conveyor belt. For upcoming field campaigns focusing on the hydrological cycle in the atmosphere, collocated lidar observations along extended flight legs could provide the large-scale horizontal moisture fluxes for specific regions in atmosphere, for example, moisture budget investigations.

REFERENCES

Boutle, I. A., R. J. Beare, S. E. Belcher, A. R. Brown, and R. S. Plant, 2010: The moist boundary layer under a mid-latitude weather system. *Bound.-Layer Meteor.,* **134,** 367–386.

Chaboureau, J.-P., and Coauthors, 2010: Long-range transport of Saharan dust and its radiative impact on precipitation forecast over western Europe: A case study during COPS. *Quart. J. Roy. Meteor. Soc.,* in press.

Didone, M., 2006: Performance and error diagnosis of global and regional NWP models. Ph.D. thesis 16597, ETH Zurich, 113 pp.

Dirren, S., M. Didone, and H. C. Davies, 2003: Diagnosis of "forecast-analysis" differences of a weather prediction system. *Geophys. Res. Lett.,* **30,** 2060, doi:10.1029/2003GL017986.

Flentje, H., A. Dörnbrack, G. Ehret, A. Fix, C. Kiemle, G. Poberaj, and M. Wirth, 2005: Water vapor heterogeneity related to tropopause folds over the North Atlantic revealed by airborne water vapor differential absorption lidar. *J. Geophys. Res.,* **110,** D03115, doi:10.1029/2004JD004957.

——, ——, A. Fix, G. Ehret, and E. Holm, 2007: Evaluation of ECMWF water vapour fields by airborne differential absorption lidar measurements: A case study between Brazil and Europe. *Atmos. Chem. Phys.,* **7,** 5033–5042.

Fritsch, J., and R. E. Carbone, 2004: Improving quantitative precipitation forecasts in the warm season: A USWRP research and development strategy. *Bull. Amer. Meteor. Soc.,* **85,** 955–965.

GLOBE Task Team, Eds., 1999: The Global Land One-Kilometer Base Elevation (GLOBE) Digital Elevation Model, version 1.0. National Oceanic and Atmospheric Administration/

National Geophysical Data Center, Boulder, CO, digital database. [Available online at http://www.ngdc.noaa.gov/mgg/topo/globe.html.]

Hoinka, K. P., and H. C. Davies, 2007: Upper-tropospheric flow features and the Alps: An overview. *Quart. J. Roy. Meteor. Soc.,* **133,** 847–865.

——, E. Richard, G. Poberaj, R. Busen, J. Caccia, A. Fix, and H. Mannstein, 2003: Analysis of a potential-vorticity streamer crossing the Alps during MAP IOP 15 on 6 November 1999. *Quart. J. Roy. Meteor. Soc.,* **129,** 609–632.

Keil, C., A. Röpnack, G. C. Craig, and U. Schumann, 2008: Sensitivity of quantitative precipitation forecast to height dependent changes in humidity. *Geophys. Res. Lett.,* **35,** L09812, doi:10.1029/2008GL033657.

Kiemle, C., G. Ehret, A. Giez, K. J. Davis, D. H. Lenschow, and S. P. Oncley, 1997: Estimation of boundary layer humidity fluxes and statistics from airborne differential absorption lidar (DIAL). *J. Geophys. Res.,* **102** (D24), 29 189–29 203.

——, and Coauthors, 2007: Latent heat flux profiles from collocated airborne water vapor and wind lidars during IHOP_2002. *J. Atmos. Oceanic Technol.,* **24,** 627–639.

Massacand, A. C., H. Wernli, and H. C. Davies, 2001: Influence of upstream diabatic heating upon an alpine event of heavy precipitation. *Mon. Wea. Rev.,* **129,** 2822–2828.

Miglietta, M. M., and R. Rotunno, 2009: Numerical simulations of conditionally unstable flows over a mountain ridge. *J. Atmos. Sci.,* **66,** 1865–1885.

Poberaj, G., A. Fix, A. Assion, M. Wirth, C. Kiemle, and G. Ehret, 2002: Airborne all-solid-state DIAL for water vapour measurements in the tropopause region: System description and assessment of accuracy. *Appl. Phys.,* **75,** 165–172.

Ralph, F. M., P. J. Neiman, and G. A. Wick, 2004: Satellite and CALJET aircraft observations of atmospheric rivers over the eastern North Pacific Ocean during the winter of 1997/98. *Mon. Wea. Rev.,* **132,** 1721–1745.

Reeves, H. D., and R. Rotunno, 2008: Orographic flow response to variations in upstream humidity. *J. Atmos. Sci.,* **65,** 3557–3570.

Richard, E., A. Buzzi, and G. Zängl, 2007: Quantitative precipitation forecasting in the Alps: The advances achieved by the Mesoscale Alpine Programme. *Quart. J. Roy. Meteor. Soc.,* **133,** 831–846.

Rotunno, R., and R. Houze, 2007: Lessons on orographic precipitation from the Mesoscale Alpine Programme. *Quart. J. Roy. Meteor. Soc.,* **133,** 811–830.

Simmons, A., and A. Hollingsworth, 2002: Some aspects of the improvement in skill of numerical weather prediction. *Quart. J. Roy. Meteor. Soc.,* **128,** 647–677.

Tollerud, E., and Coauthors, 2008: Mesoscale moisture transport by the low-level jet during the IHOP field experiment. *Mon. Wea. Rev.,* **136,** 3781–3795.

Weissmann, M., F. J. Braun, L. Gantner, G. J. Mayr, S. Rahm, and O. Reitebuch, 2005a: The Alpine mountain–plain circulation: Airborne Doppler lidar measurements and numerical simulations. *Mon. Wea. Rev.,* **133,** 3095–3109.

——, R. Busen, A. Dörnbrack, S. Rahm, and O. Reitebuch, 2005b: Targeted observations with an airborne wind lidar. *J. Atmos. Oceanic Technol.,* **22,** 1706–1719.

Wernli, H., and H. C. Davies, 1997: A Lagrangian-based analysis of extratropical cyclones. I: The method and some applications. *Quart. J. Roy. Meteor. Soc.,* **123,** 467–489.

Wirth, M., A. Fix, P. Mahnke, H. Schwarzer, F. Schrandt, and G. Ehret, 2009: The airborne multi-wavelength water vapor differential absorption lidar WALES: System design and performance. *Appl. Phys.,* **96B,** 201–213.

Wulfmeyer, V., and Coauthors, 2008: The convective and orographically induced precipitation study: A research and development project of the World Weather Research Program for improving quantitative precipitation forecasting in low-mountain regions. *Bull. Amer. Meteor. Soc.,* **89,** 1477–1486.